Deformation of soap bubbles in uniform electric fields

S. Mawet,* H. Caps, and S. Dorbolo
GRASP Lab, CESAM Research Unit, University of Liège, B-4000 Liège, Belgium

(Received 30 November 2020; accepted 6 April 2021; published 27 April 2021)

The deformation of hemispherical bubbles under vertical static electric fields was studied using a plane capacitor. The deformation and the bubbles shape have been monitored according to the amplitude of the electric field and the initial volume of the bubbles. Two different substrates, a dry solid plate or a liquid pool, were used to inspect the influence of the pining of the contact line. The deformation of sessile (on dry solid plate) and floating (on a liquid pool) bubbles were compared. The deformation parameter has been rationalized using a simple model. More precisely, the number of interfaces has been found to be a relevant parameter that imposes the shape of the bubbles.

DOI: 10.1103/PhysRevFluids.6.043603

I. INTRODUCTION

The fate of charged bubbles is intimately related to that of charged droplets. The main difference resides in counting the number of interfaces that separate the liquid and the gaseous phases. We will start by introducing what was done on charged droplets before focusing on the case of charged bubbles.

Numerous phenomena originate from the combined effects of the electric field and the surface tension at liquid interfaces. According to Sartor [1], Franklin was one of the first to suggest that rain can be due to the attraction of opposite charged droplets. Moreover, charged droplets have a crucial role in the establishment of strong electric fields in thunderstorms [1–3] or in the creation of preferred paths for lightning strikes [4,5]. Due to there essential impact on weather, the charged droplets and their disintegration were abundantly studied. Early, Lord Rayleigh made some fundamental experiments on drop coalescence in an electric field [6] and calculated the maximal charge that a spherical droplet can hold [7]. He showed that the droplet destabilization is related to a dimensionless number, the fission ratio, $\mathrm{X} = q^2/(64\pi^2\varepsilon_0\gamma r^3)$ for a spherical droplet of radius r, made of a liquid with a surface tension γ, carrying a charge q in a medium of permittivity close to the one of the vacuum ε_0. This dimensionless number results from the balance between the electric pressure $P_e = q^2/(64\pi^2\varepsilon_0 r^4)$ and the capillary pressure $P_c = 2\gamma/r$ at the surface of a spherical charged droplet. If $\mathrm{X} \geqslant 1$, then the electric pressure surpasses the capillary one and the droplet becomes unstable, deforming into a spheroid and emitting thin charged jets along its major axis. This phenomenon has been confirmed experimentally by Duft *et al.* [8,9]. Moreover, experiments performed by Pelesz [10] on pendant bubbles indicate that the maximum carried charge is similarly predicted by the fission ratio X.

At the beginning of the last century, Zeleny studied the dynamics of a droplet resting at the tip of a liquid-filled tube charged upon application of an high voltage [11–13]. He observed the deformation of the droplet from a hemispherical shape into a hemispheroidal one. Above some critical threshold, the instability is triggered and the subsequent emission of microscopic liquid jets is observed. This phenomenon is known as electrospray [13]. The same study proposed a law for the stability of

*smawet@uliege.be

a hemispheroidal droplet charged upon application of an electric voltage [11]. Later, Taylor [14] found that the spheroidal approximation remains valid only at the early stage of the deformation. Just before the instability, he observed that the shape of the droplet is close to a cone. This led him to the deduction of a new stability law [14]. Thanks to this discovery, the instability is still known today as the Taylor's cone.

In the same article, Taylor proposed a stability limit for an initially uncharged droplet under an electric field assuming that the resulting polarization causes the droplet to deform into a prolate spheroid [14]. Basaran *et al.* used a numerical approach to study the shape of a charged droplet with [15] and without [16] electric fields. They also predicted the stability of those shapes thanks to the bifurcation theory. In particular, they found that the deformation into an oblate spheroid is stable for a charged droplet beyond the Rayleigh limit in absence of electric fields [16]. Furthermore, under electric field, the charged droplet loses its equatorial symmetry and adopts an egg shape with the egg tip pointing in the direction of the electric field [15]. They applied the same method to study the deformation of a resting (or pendant) conducting droplet under a uniform electric field [17]. In the case of small deformations, the aspect ratio of the droplet (the height of the droplet H_d divided by its base radius r) can be linked with the intensity of the uniform electric field E_0. For a hemispherical droplet with an initial radius r_0 and a fixed contact angle in a dielectric medium of permittivity ε, the law writes as

$$\frac{H_d}{r} = 1 + \frac{9}{4}\mathrm{Bo}_{e,d}, \tag{1}$$

where $\mathrm{Bo}_{e,d} = \varepsilon E_0^2 r_0/2\gamma$ is the electrical Bond number, balancing electrostatic and capillary pressures.

In a more recent article, Beroz *et al.* [18] found, both experimentally and analytically, a law linking $\mathrm{Bo}_{e,d}$ and the critical aspect ratio of a droplet, corresponding to the static aspect ratio of a droplet under conditions just below the ones needed to trigger the instability. Those experiments were performed for a hemispherical conducting pendant droplet pinned on a conducting surface and submitted to a uniform electric field. They eventually came up with the law $r^3/v = \pi/2\,\mathrm{Bo}_{e,d}$ for the droplet critical aspect ratio, where v is the initial volume of the drop. In another recent article, Wagoner *et al.* [19] numerically studied the shape and the stability of a droplet submitted to a uniform electric field and having a lower conductivity and permittivity than the surroundings fluid. According to the viscosity ratio between the droplet and the surrounding fluid, the authors found two kinds of shapes adopted by the droplets when the intensity of the electric field increase: dimpled and lens. They observed that lens shaped drops (prettily called "Saturnian droplet" by Marin [20]) can undergo an instability similar to the Taylor cone (but involving in completely different mechanisms): equatorial streaming, already experimentally observed by Brosseau *et al.* [21].

Although the interest in charged droplets was initially driven by their crucial role in weather, they have numerous other applications. In multiphasic systems composed of a continuous liquid phase and a dispersed one (made of gas bubbles or liquid droplets), the mass and heat transfer rates are proportional to the interfacial surface area. The use of an electric field to increase the interfacial area by deforming (or even disintegrating) the dispersed phase is supposed to enhance both transfer rates [22,23]. The electrospray and the electrospinning were also studied for their ability to generate micrometric droplets of controlled sizes or ionized mist [24–26] and nanofibers [27]. The large amount of applications ranges from high-resolution printing [28] to space propulsion [29] via droplets encapsulation [30] or wound healing [31].

Compared to this abundance of researches on droplets, air bubbles are poorly documented. Indeed, bubbles have been early used experimentally to determine scaling laws for the critical field intensity, i.e., the minimum field needed to trigger the Taylor cone [see Fig. 1(c)] [32,33]. However, since those initial studies, bubbles have been seen as a particular cases of droplets with two interfaces instead of one [17,18]. Nevertheless, they have their own peculiarities as observed by Hilton *et al.* [34] on bubbles charged upon application of a voltage triggering the Taylor cone. Moulton *et al.* [35] also studied the stability under an electric field of a closely related system consisting of a soap

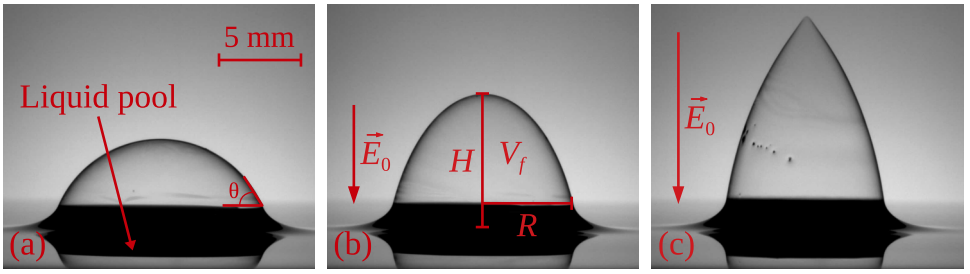

FIG. 1. Pictures of a bubble floating on a soap pool under a uniform electric field. The picture (a) shows the bubble on a liquid pool when the intensity of the electric field $E_0 = 0$. (b) Deformation of a bubble induced by the uniform electric field. The bubble adopts a hemispheroidal shape when $E_0 < E_T$ with E_T the intensity needed to trigger the instability. (c) When $E_0 > E_T$, the instability occurs, the bubble becomes pointy and starts to eject droplets to the top plate to discharge. This behavior is called the Taylor cone. The height H and the radius R of the bubble as well as the emerged volume V_f and the apparent initial contact angle θ of the bubble are measured.

film membrane of catenoidal shape. The soap film was assembled like a cylindrical capacitor with a voltage between a metallic rod situated along the radial axis of the catenoid and the catenoid itself, which was grounded. Like the bubbles of spheroidal shape, the soap film was attracted by the central electrode and, therefore, was deformed upon application of an electric field.

One of the aspect that has been overlooked so far is the interaction of the bubbles with the substrate that we investigate in the present study. Indeed, the initial shape of droplets depends on the wetting and therefore on the contact line, i.e., the meeting point between the solid, the liquid and the gaseous phases. The contact angle of the droplets with the substrate can range between 0° (total wetting) and 180° (superhydrophobic). However, the situation is different for bubbles; as a matter of fact, on a dry plate the bubbles adopt a hemispherical shape, with a apparent contact angle of 90°. If deformed, then the bubbles may be frustrated due to the contact line hysteresis, potentially like sessile droplets. Moreover, if the plate is replaced by a pool, then the apparent contact angle between the bubbles and the pool depends on the volume of the bubble [36].

Our aim is to describe the deformation of bubbles under uniform electric fields with a special focus set on the influence of substrates. Up to now, studies on sessile bubbles dealt with the mobility of the contact line by wetting the solid surfaces [17,32,33]. However, wetting the solid surfaces only allows for a partial control of pinning of the contact line. In this article, we compare the deformation induced by an electric field on bubbles resting on a dry surface as well as on bubbles floating on a soapy bath (see Fig. 1) to inspect the influence of the pinning on the deformation. On the pool, a new question arises: do the immersed part of the floating bubble influences the deformation? Similar experiments on floating bubbles have been performed by Macky [33]. The resulting effect of the substrate remained unsettled. This is mainly because the pool of soapy solution was considered as a convenient way to feed the Taylor cone in liquid (to study it longer) rather than a real parameter of the experiment.

Beyond the academical interest in studying the combined effects of the electric field and the surface tension at bubbles surface, there are also numerous applications of electrified soap bubbles and films. The work of Moulton *et al.* [35], for example, points out that the spheroidal shape of a bubble is only one of the wide range of shapes that soap film can achieve. This leads to expect that electrified soap film could be adapted in many more configurations than liquid droplets with all the potential applications that may result from this adaptability. Moreover, Bonhomme *et al.* [37] showed that when a field is applied between the bottom and the top of a cylindrical soap film, an electro-osmotic flow is induced. This flow counteracts the natural drainage, increasing the lifetime of the film. As similar flows can be observed in electrified soap bubbles, a better understanding of those bubbles should allow a better control of their lifetime. Additionally, as it was pointed

out by Loscertales *et al.* [30], coaxial electrospray can be used to produce encapsulated droplets. Understanding how, and under which conditions, this technique could be extended to bubbles to generate micrometric bubbles of controlled size should have a considerable interest to achieve homogeneous foam. Another possibility to reach this goal is to use the peculiar instability observed by Hilton *et al.* [34]. Electrified soap bubbles also appears to be a promising way to generate highly charged aerosols thanks their bursting and the subsequent emission of charged droplets [38].

The experimental setup is presented in Sec. II. We first explore the time dependency of the height of the bubbles to properly define the steady state (Sec. III). Then, the height is measured as a function of the applied electric field for a sessile bubble on a dry surface (Sec. IV) and a floating one on a soap pool (Sec. V). The results are compared and discussed. The liquid bath depth is then considered. The partially immersed bubble is viewed as a floating but frustrated bubble (Sec. VI). A general conclusion is drawn in Sec. VII.

II. EXPERIMENTAL SETUP

The experiments were carried out under a uniform electric field generated by a plane capacitor made out of two rectangular aluminum plates (70 mm $\times$ 100 mm surface and 5 mm thickness). The bottom electrode of the capacitor, which was grounded, was also used as substrate for the bubble. This electrode may be immersed in a liquid bath contained in a Petri dish of 70 mm radius and 10 mm depth filled to the brim. The bath is made of the same mixture as the bubbles. This setup enabled us to perform experiments on sessile bubbles resting on a dry aluminum plate as well as on bubbles floating on a soap pool. The distance between the immersed electrode and the liquid surface, labeled e, was controlled by modifying the position of this electrode in the bath. A high voltage DC power supply (PS375 Stanford research systems) was used to apply voltage between the plates. This generator can reach a voltage up to 20 kV. The generator was controlled using a Python program through a GPIB bus. This program was also used to acquire the images from a camera (Thorlabs USB model). The top plate was supported by a Perspex frame allowing us to vary the distance between the liquid surface and the top electrode ($d = 15,\ 20,$ and 25 mm) as well as the distance between electrodes $d_t = d + e$ (in absence of bath, $d_t = d$ as $e = 0$). Sketches of the experimental setup are shown in Fig. 2.

Bubbles were blown from a surfactant mixture based on the stock solutions formulated in Ref. [39]: the stock solution was composed of 6.6 wt % of sodium lauryl-dioxyethylene sulfate (SLES from Stepan Company) and 3.4 wt % of cocoamidopropyl betaine (CAPB from Evonik Industrie). Next, 0.4 wt % of myristic acid (MAc from Roth Carl) was dissolved by heating the mixture up to 60 °C. To increase the viscosity of the mixture, the stock solution was diluted 10 times in a mixture 60 wt % of glycerol (from Sigma-Aldrich) and 40 wt % of distilled water. The physical properties of the resulting solution were measured: we found a viscosity $\eta = 10.5$ mPa s at 22 °C according to a Haake MARS III rheometer, a surface tension $\gamma = 21.6$ mN/m thanks to the pendant drop method [40] (CAM 200 model from KSV Instrument) and a density $\rho = 1.03\ 10^3$ kg/m^3. This solution allows us to obtain bubbles that may last for hours.

A syringe pump was used to inflate the bubbles. On a dry surface, a 20 μl droplet of soapy solution was released on the bottom electrode with a micropipette and then the bubble was inflated. On a bath, the air was directly injected under the surface to create the floating bubbles. The time required to inflate the bubbles and to start the experiment was roughly 10 s. This protocol allowed to control the gas volume ($V_g = 1,\ 0.5,$ and 0.25 ml) in the bubble and therefore the typical size of the bubble. Nevertheless, the final volume was not reproducible because of leaks and air compressibility. Therefore, the precise volume was obtained *a posteriori*, after the generation of the bubble. In the case of floating bubbles, the observed volume differs from V_g since a part of the bubbles is immersed. Indeed, as we analyzed a side view of the scene, only the emerged part V_f could be directly measured. Those measurements, plus the height and the radius of the bubble, respectively labeled H and R, were performed by a homemade Python program detecting the edge and the meniscus of the bubbles. Note that R was measured at the top of the meniscus [see Fig. 1(b)].

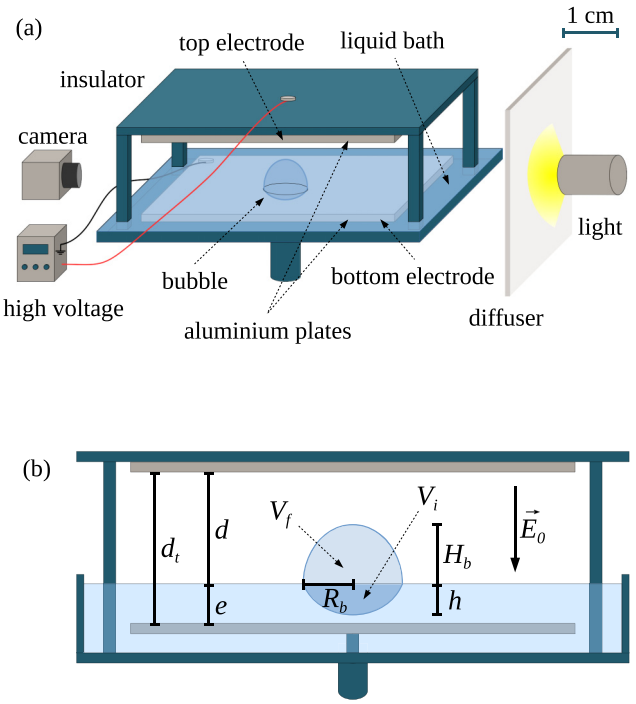

FIG. 2. Sketches of the experimental setup used for the experiments performed on floating bubbles. (a) Plan of the elements composing the experimental setup. (b) Drawing of the geometrical measures of the experiment: the liquid depth e between the immersed electrode and the liquid surface, the size of the capacitor d, the distance between electrodes d_t, the electric field $\vec{E}_0$, the penetration depth h, the height H_b and the radius R_b (measured at the top of the meniscus) of the bubble as well as its emerged and immersed volume V_f and V_i. The scale of both sketches is the same and is indicated in the top right corner.

The typical error linked to the measurements of H was due to the picture resolution (which correspond roughly to the size of a pixel that is about 10 μm in actual length) as well as the bubbles base detection. In the worst-case scenario, the variation on the base detection was accurate within about ten pixels. Moreover, the apex of the bubble was inferred by adjusting a circle on the top part of the bubbles edge and thus had subpixel accuracy. Consequently, the standard error on the absolute value of H was mainly due to the base detection and corresponds, at worse, to 100 μm. Beside, the typical error linked to the measurements of R also depended of the picture resolution, but, unlike H, was related to the detection of the top of the meniscus, which was even more accurate than the base detection (namely, two or three pixels). As R was obtained by measuring the distance between both intersections of the meniscus top and the detected edges, the standard error on R was smaller than the one on H. This corresponds to a characteristic relative error of a few percents or less for both H and R. Moreover, by propagating the uncertainty, the maximal relative error of the ratio H/R can be deduced to be of the same order of magnitude than the one linked to H, namely, two or three percents.

As the mean typical thickness of a bubble can be estimated at a few microns or less [41], we can assume that the bubble shape is not affected by gravity [42]. Moreover, the estimated liquid conductivity $\sigma > 5.5\ 10^{-6}$ S/m and permittivity $\varepsilon \approx 80\varepsilon_0$ with $\varepsilon_0 \approx 8.85\ 10^{-12}$ F/m the permittivity of free-space, allow for estimating the characteristic electric relaxation time $\tau_{e,l} = \varepsilon/\sigma < 1.29\,10^{-4}$ s. Beside, the gas surrounding the bubble is air ($\tau_{e,g} = \varepsilon_0/\sigma_g \sim 10^3$ s, where $\sigma_g \sim 8\ 10^{-15}$ S/m [43]) and the characteristic time of the experiment $t_{\text{step}} \sim 10^1$s. Therefore, the bubble and the soap pool

used for the experiments performed on floating bubbles can be regarded as perfect conductors [44]. Consequently, the actual bottom electrode of the capacitor in the experiments performed on floating bubbles is defined by the surface of the liquid pool and therefore, the capacitor had a size d.

The experiments were performed by increasing the voltage ϕ by steps of ϕ_{step} every duration t_{step} from ϕ_{min} to ϕ_{max} and by recording the successive deformations with a camera. All experiments were performed at least twice. As a plane capacitor is used, an increase of the voltage results in a growth of the intensity of the uniform electric field $E_0 = \phi/d$ inside the capacitor. A systematic error arises from the uncertainty on d (estimated equal to 0.5 mm) which affect equivalently all the absolute value of E_0, but have no effect on the general appearance of the curves. A picture of the bubble was taken at the end of each step, i.e., just before the change of voltage. A 20 s delay was imposed before each experiment to minimize temporal effects due to the initial aging of the bubble. The DC power supply controlled the voltage with an accuracy of the order of 1 V and allowed a maximum current of 525 μA. It took approximately 1 s to reach the voltage setpoint independently of the change in voltage and of the voltage itself.

III. STEADY STATE

When a voltage is applied, it takes some time for the bubble to stabilize and reach a new steady state. To estimate this duration, we applied a high voltage and we tracked the height of the bubble H as a function of time. The height H is defined as the semimajor axis of the hemispheroid formed by the bubble. This experiment was performed with a floating bubble of $V_g = 0.5$ ml inside a capacitor of $d = 20$ mm. At $t < 0$ s, the DC power supply was off and the voltage between the liquid pool and the top plate was null. At $t = 0$ s, the generator was switched on and, within the next second, the top plate was set to 9 kV (a voltage very close to the one required to trigger the Taylor cone). In Fig. 3, H is reported as a function of time in a spatiotemporal diagram. The shapes of the bubble in the initial and final situations are, respectively, shown as insets (i) and (ii) in Fig. 3. The required time needed to reach a steady height H_b is linked to a characteristic time τ_c. Since the pressure constraints vary with the bubble shape, this characteristic time τ_c was obtained by fitting (black line in Fig. 3) a stretched exponential function [45]:

$$H(t) = H_b - D\exp\left[-\sqrt{(t/\tau_c)}\right]. \tag{2}$$

We note D the amplitude of the deformation of the bubble, i.e., the difference between H_b and the initial height H_0, and $\tau_c \simeq 5$ s the characteristic time of the deformation process. Both the characteristic time and the deformation depend on the change in voltage and the initial voltage itself. We ensured that at least 90% of the deformation was achieved, and hence that H_b was reached, by waiting at least $5\tau_c$ between two changes of the setpoint. In Fig. 3, we presented the maximum change achieved before reaching the Taylor cone's voltage. In practice, the changes were $\phi_{\text{step}} = 100$ V every $t_{\text{step}} = 10$ s, which is smaller than the one illustrated in Fig. 3. Consequently, $\tau_c < 1$ s, the condition $t_{\text{step}} > 5\tau_c$ was almost always satisfied and we considered that the quasistatic shapes of the bubbles were recorded. Therefore, the steady height H_b and radius R_b of the bubbles were measured at the end of each time step.

In Fig. 4, two typical measurements of H_b when ϕ and then E_0 were increased are reported: one on a dry surface (red points) and the other on a liquid pool (blue points). The voltage was increased by steps of 100 V every 10 s from $\phi_{\text{min}} = 0$ V to $\phi_{\text{max}} = \phi_T$, a voltage close to that of the onset of the Taylor cone. In both cases, $V_g = 0.25$ ml and $d = 25$ mm. Pictures (i) and (ii) in Fig. 4 show the bubbles when $E_0 = 0.02$ kV/mm in both situations. Pictures (iii) [respectively, (iv)] in Fig. 4 illustrate the deformation of the bubbles resting on a solid when $E_0 = 0.46$ kV/mm (respectively, floating on a liquid when $E_0 = 0.52$ kV/mm). Two major differences can be noticed. First, the bubble height H_b is substantially smaller for a floating bubble, even without any applied field. Second, to obtain the same deformation D on a floating bubble, it is necessary to apply a stronger field (that is to say, a stronger voltage). The explanations for these differences are developed in the next sections. Those examples included, H_b and R_b were measured according to the increasing

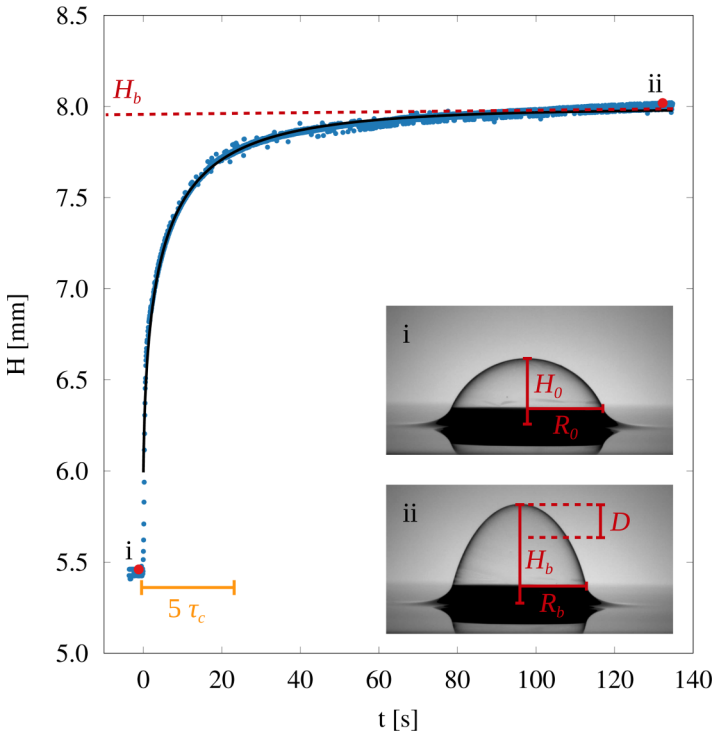

FIG. 3. Height of the floating bubble H as a function of time. The size of the capacitor was $d = 20$ mm and the volume of the bubble was $V_g = 0.5$ ml. At time $t = 0$ s the DC supply was set on and the top plate reached the preset voltage. Here, only one step is needed to go from 0 kV [on picture (i)] to 9 kV [on picture (ii)]. The black line is the fitting function, described by Eq. (2), used to obtain the characteristic time τ_c and deformation D as well as the steady height H_b and radius R_b. The τ_c for this experiment was found equal to 4.7 s.

voltage for eighteen combinations of the parameters: three capacitor gaps ($d = 15,\ 20,$ and 25 mm) and three bubble air volumes ($V_g = 1,\ 0.5,$ and 0.25 ml) for both sessile and floating bubbles.

IV. SESSILE BUBBLES

Taking advantage of their cylindrical symmetry, the shape of sessile bubbles can be fully characterized by two geometric parameters. We chose the stationary height H_b and the stationary radius measured at the top of the meniscus R_b (see Fig. 3). Furthermore, energy in the system come from two contributions: the electrostatic energy due to the presence of the bubble in the electric field and the surface energy due to capillarity. As the bubble adopts a hemispheroidal shape, the two contributions are respectively proportional to $E_e \propto -\varepsilon_0 E_0^2 R_b^3$ and $E_c \propto 2 n_f \gamma R_b^2$, with n_f the number of interfaces and γ the surface tension per interface. Consequently, H_b can be expressed as a function of five-dimensional governing parameters, which are R_b, γ, n_f, ε_0, and E_0. Four of those have independent dimensions and the dimension of the fifth one can be expressed as a product of the others. If the dimension of ε_0 is chosen as the dependant one, then it can be formulated as

$$[\varepsilon_0] = [\gamma][n_f][R_b]^{-1}[E_0]^{-2}. \tag{3}$$

Beside, the dimension of H_b can also be expressed as a product of the dimensions of the four same dimensional parameters. Therefore, the following relation can be written according to the dimensional analysis and the Buckingham Π theorem [46],

$$\mathrm{Ar_s} = f_s(\mathrm{Bo}_{e,s}), \tag{4}$$

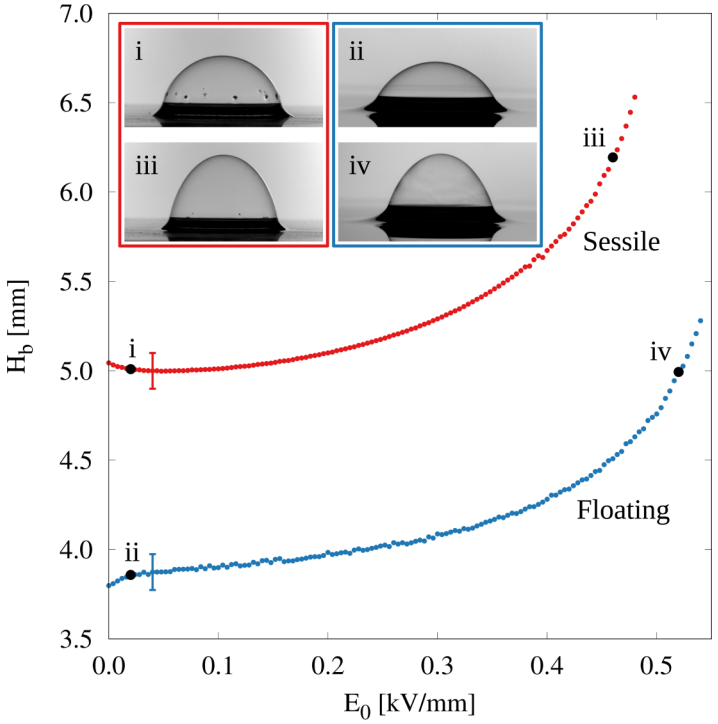

FIG. 4. Stationary height of bubbles H_b at different intensity values of the applied fields E_0. Both curves correspond to bubbles of $V_g = 0.25$ ml and a capacitor of $d = 25$ mm. The red and the blue points are respectively for a bubble on solid and liquid substrate. Pictures (i) and (ii) illustrate the shape of a bubble under $E_0 = 0.02$ kV/mm for a solid (i) and a liquid (ii) substrate. Pictures (iii) and (iv) show the deformation of a bubbles respectively resting on solid, under $E_0 = 0.46$ kV/mm and floating on a liquid under $E_0 = 0.52$ kV/mm. A typical error bar, corresponding to the worst-case scenario, is indicated on each curve.

with $\mathrm{Ar}_s = H_b/R_b$ the aspect ratio and $f_s(\mathrm{Bo}_{e,s})$ a function of $\mathrm{Bo}_{e,s} = \varepsilon_0 E_0^2 R_b/4\gamma$ the energies ratio, i.e., the electrical Bond number. The factor 4 in $\mathrm{Bo}_{e,s}$ comes from E_c and should be taken into account since we have two interfaces ($n_f = 2$) and a cylindrical symmetry. This definition is similar to Basaran's definition [17].

In Fig. 5, the aspect ratio $\mathrm{Ar_s}$ is plotted as a function of $\mathrm{Bo}_{e,s}$ in the dry case. Three sizes of capacitor and three internal volumes are presented. On top of that, data obtained by Basaran *et al.* [17] are represented (black bullets). Both results are very similar even if we used smaller bubbles (three to five times smaller) and capacitors (three to six times smaller). This good agreement between all results in a large range of parameters indicates that sessile bubble shapes are pretty well described by $\mathrm{Ar}_s(\mathrm{Bo}_{e,s})$. In addition, the energy ratio $\mathrm{Bo}^*_{e,s}$ required to trigger the bubble instability (i.e., to start the Taylor cone) is the same in all cases. The small deformations are well predicted by the law $\mathrm{Ar}_s = 1 + 9/4\,\mathrm{Bo}_{e,s}$, adapted from Eq. (1) [17] (continuous black line in Fig. 5).

V. FLOATING BUBBLES

A. Differences with sessile bubbles

As mentioned in Sec. III, there are two major differences between a bubble resting on a dry solid plate and a bubble floating on a liquid bath when they are submitted to an electric field. This is essentially due to pinning of the contact line and to the partial immersion. This will be discussed on the basis of Fig. 6, which presents the aspect ratio $\mathrm{Ar}_s = H_b/R_b$ for floating (in green, orange

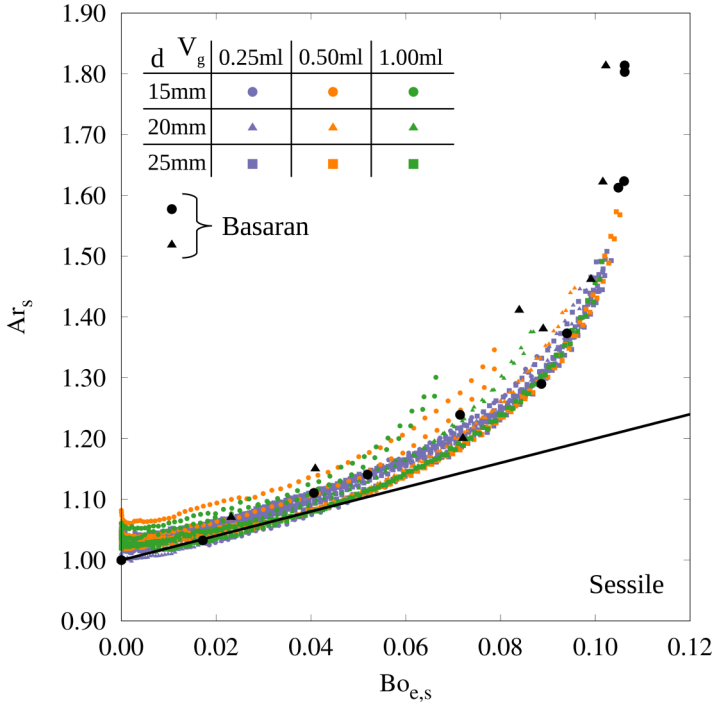

FIG. 5. Aspect ratio of sessile bubbles $\mathrm{Ar}_s = H_b/R_b$ resting on a dry solid plate plotted as a function of the energy ratio $\mathrm{Bo}_{e,s} = \varepsilon_0 E_0^2 R_b/4\gamma$. Three sizes of capacitors d have been used: $d = 15$ mm (solid circles), 20 mm (solid triangles), and 25 mm (solid squares), as well as three internal volumes V_g: $V_g = 0.25$ ml (in mauve), 0.50 ml (in orange), and 1.00 ml (in green). The black bullets represent the data presented from Ref. [17] for a capacitor of $d = 85.5$ mm and an approximate internal volume of $V_g = 35.14$ ml (solid circles) or $V_g = 30.05$ ml (solid triangles). The black straight line correspond to the small deformations law adapted from Eq. (1). On this graphic and the following ones, error bars are smaller than the bullets.

and mauve) and sessile bubbles (in red) as a function of $\mathrm{Bo}_{e,s}$. The two major differences are the following. First, the height of the bubble H_b and therefore the aspect ratio Ar_s are substantially smaller for floating bubbles, even without any applied field. Second, to obtain the same deformation D on floating bubbles, it is necessary to apply higher field and consequently to reach higher $\mathrm{Bo}_{e,s}$.

B. Aspect ratio modification

The aspect ratio measurement need to be adapted for the case of floating bubbles. Indeed, the interaction between a bubble and a liquid pool has a major impact on the bubble shape. The initial shape can be characterized by measuring θ, the apparent contact angle between the top of the meniscus and the edge of the bubble [see Fig. 1(a)]. In practice, we measured $\theta = 90^\circ$ for sessile bubbles and $\theta \sim 60^\circ$ for floating ones. It is possible to show that, initially, $R_c = R_b/\sin(\theta)$ with R_c the radius of curvature. Therefore, while $R_c \approx R_b$ for sessile bubbles, this is not true anymore for floating ones. As the capillary energy directly depends on R_c, the energy ratio for floating bubble is written as $\mathrm{Bo}_e = \varepsilon_0 E_0^2 R_c/4\gamma$ with $R_c = R_b/\sin(\theta)$. Moreover, to keep only one length scale, the aspect ratio is accordingly written as $\mathrm{Ar} = H_b/R_c$. The factor $\sin(\theta)^{-1}$ is a convenient way to take into account that the initial shape of the emerged part of the floating bubble is not a hemisphere, but a spherical cap.

Furthermore, a part of the floating bubble is immersed and this has an effect on the initial aspect ratio. The measured initial aspect ratios $\mathrm{Ar}(E_0 = 0)$ are compared to those obtained by Teixeira

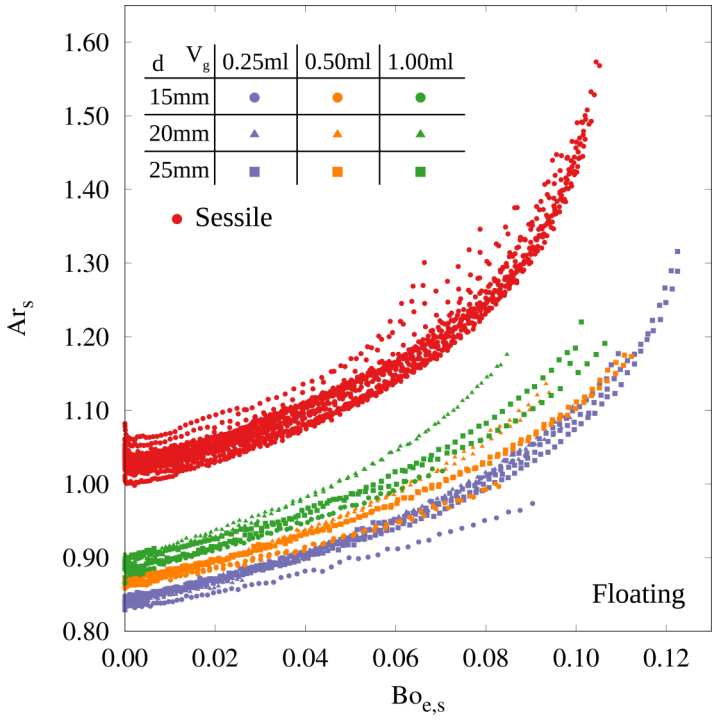

FIG. 6. Aspect ratio of floating bubbles $\mathrm{Ar}_s = H_b/R_b$ as a function of the energy ratio $\mathrm{Bo}_{e,s} = \varepsilon_0 E_0^2 R_b/4\gamma$. The same three sizes of capacitors d had been used: $d = 15$ mm (solid circles), 20 mm (solid triangles) and 25 mm (solid squares), as well as the same three internal volumes V_g: $V_g = 0.25$ ml (in mauve), 0.50 ml (in orange), and 1.00 ml (in green). The results for bubbles resting on a solid substrate (red solid circles) are drawn for the sake of the comparison.

et al. [36] in Table I. The authors showed that the floating bubbles could be organized into three categories based on their size and the buoyancy Bond number Bo_b. This dimensionless number accounts for the balance between the gravitational energy due to the buoyancy acting on a fully immersed bubble $E_b \propto g\rho_g R_c^4$ with $\rho_g = 1\,\mathrm{kg/m^3}$, the density of the air and the capillary energy due to the interface between the fully immersed bubble and the bath E_c. For a large $\mathrm{Bo}_b = g\rho_g R_c^2/\gamma$, the buoyancy completely overcomes the capillarity and the bubble almost entirely emerges. However, for small Bo_b, the capillarity entirely dictates the behavior of the bubble which slightly emerges from the pool surface with a shape that closely resembles that of on immersed sphere. Between those two limiting cases, the intermediate regime is characterized by a moderate Bo_b. This means that the bubbles have enough gravitational energy to emerge from the bath, but not enough to completely neglect the effect of minimization of the surface due to capillarity.

TABLE I. Comparison between our measured initial aspect ratios $\mathrm{Ar} = H_b/R_c$ (when $E_0 = 0$) and the theoretical ones obtained by Teixeira *et al.* [36] for the three different internal volumes V_g considered. The predicted immersed parts of the bubble represented by h/R_c, are also given.

V_g [ml]	$\mathrm{Ar}(E_0 = 0)$	$\mathrm{Ar}(E_0 = 0)$ [36]	h/R_c [36]
1.00	0.80	0.76	0.22
0.50	0.75	0.73	0.26
0.25	0.70	0.69	0.31

All the bubbles used in our experiments have a size corresponding to a moderate Bo_b and therefore belong to the intermediate regime. This means that both the immersed and the emerged parts of the bubbles have an impact on the bubble shape and cannot be neglected. In this case, the immersed parts of the bubble represented by h/R_c, with h the penetration depth, are about 31% for a bubble of $V_g = 0.25$ ml ($\mathrm{Bo}_b \approx 9.92$) to 22% for a bubble of $V_g = 1$ ml ($\mathrm{Bo}_b \approx 15.46$) (see Table I).

C. Energy modification

The change in aspect ratio allowed us to rationalise why $\mathrm{Ar}(E_0 = 0) \neq 1$ for floating bubbles, but not to explain why higher electric fields are required to obtain the same deformations D as on sessile bubbles. It can be understood by remembering that a bubble on a dry solid has two interfaces, that contribute equivalently to the capillary energy ($n_f = 2$ for a sessile bubble). For floating bubbles, there is an additional interface between the liquid pool and the immersed part of the bubble. In general, this interface does not have the same R_c as those of the other interfaces. Consequently, the capillary energy is given by $E_c = (2n_f\gamma/R_c)V_f + (2n_i\gamma/R_i)V_i$, where R_c, V_f, n_f are, respectively, the emerged radius of curvature, the bubble air volume and the number of interfaces (which is equal to two). R_i, V_i, and n_i are the corresponding parameters for the immersed part of the bubble (with $n_i = 1$). Although the shape of the emerged part is a spheroidal cap and $V_f \propto R_c^3$, this is not generally the case for the immersed part. However, as it has been showed by Teixeira *et al.* [36], the shape of the immersed part of a floating bubble is completely prescribed by Bo_b. Consequently, if γ, ρ_g, and g are constant, then the immersed shape of the bubble is a complex function of R_c. Therefore, the capillary energy of a floating bubble can be written as

$$E_c \propto 2\gamma R_c^2[2 + \xi(R_c)], \tag{5}$$

where $\xi(R_c) \propto V_i/(R_i R_c^2)$ is a dimensionless function describing the relative importance of the immersed part comparatively to the emerged one.

As showed in Ref. [36], it is possible to sort floating bubbles in three categories according to Bo_b, the buoyancy Bond number. In the limit of large Bo_b, the bubble almost entirely emerges, its bottom is flat ($R_i = \infty$) and $V_i \to 0$. Therefore, the contribution of the immersed interface to the capillary energy is null and $\xi \to 0$. In this limit case, the floating bubble should have the same behavior as a sessile bubble on a solid surface. However, when Bo_b is small, the bubble slightly emerges from the surface ($V_i \to V_g$) and we can then consider $R_c/R_i \approx 2$ [47]. This result is obtained by neglecting the hydrostatics pressure from the liquid. Champagne bubbles, which have $R_i = 0.5$ mm, are a typical example of this behavior [47]. In this limiting case, the capillary energy is almost completely determined by the immersed part of the bubble (as $\xi \gg 2$). As explained in the last subsection, the bubbles used in our experiments are just between both limiting cases. In Ref. [36], the shape of intermediate size bubbles is almost symmetric about a horizontal plane situated just below the top of the capillary meniscus. Consequently, $\xi \approx 1$ and we assume that each interface brings the same amount of capillary energy, which is reasonably approximated by $E_c \propto 2n\gamma R_c^2$ with $n = n_f + n_i = 3$ the total number of interfaces.

Now, let us consider the electrostatic energy due to the presence of the bubble in the electric field. It is similar for the solid and the liquid substrates. Indeed, $E_e = -\vec{P}.\vec{E}_0/2$ with $\vec{P}$ the dipole moment due to the electric field $\vec{E}_0$. The charges are located on the outer faces of both floating and sessile bubbles (or of sessile droplets) since bubbles act like a perfect conductor and therefore, behave like Faraday cages. Consequently, there is no field in the bubbles and therefore no charge along the inner faces. Moreover, $\vec{P} = \alpha\vec{E}_0$, with α the polarizability. For a conducting hemisphere, $\alpha = 3\varepsilon_0 V_f$ with $V_f = V_g$ the volume of the hemisphere. However, for a very thin conducting spherical cap ($Ar_i \ll 1$ and $\varepsilon \gg \varepsilon_0$), $\alpha = \varepsilon_0 V_f$ [48]. The assumption on the particle size in Ref. [48] is satisfied as the external electric field is constant. Floating bubbles lie between these two limit cases: their aspect ratio close to one (see Table I) should cause α to be close to that of a hemisphere. At first sight, E_e can then be assumed independent of the shape. Therefore, the electrostatic energy is well approximated by $E_e \propto -\varepsilon_0 E_0^2 R_c^3$.

D. New dimensional analysis

Let us now focus on the description of the shape of floating or sessile bubbles in terms of dimensionless numbers. In addition to the five initial dimensional governing parameters used in the first dimensional analysis [see Eq. (3)], we should add the ones seen in the last subsection. This leads to define H_b as $f(R_c, \gamma, n, \varepsilon_0, E_0, g, \rho_g)$. Only five of them have independent dimensions. Beside ε_0, the dimension of any other parameter can be expressed as a product of the dimension of the remaining parameters. If the dimensions of ε_0 and ρ_g are chosen as the dependant ones, then they can be formulated as

$$[\varepsilon_0] = [\gamma][n][R_c]^{-1}[E_0]^{-2}[g]^0, \tag{6}$$

$$[\rho_g] = [\gamma][n][R_c]^{-2}[E_0]^0[g]^{-1}. \tag{7}$$

The dimensions of H_b can also be expressed as a product of the dimensions of the five same dimensional parameters. Then, according to the dimensional analysis and the Buckingham Π theorem [46], the following relation holds:

$$\mathrm{Ar} = f(\mathrm{Bo}_b, \mathrm{Bo}_e), \tag{8}$$

with $\mathrm{Ar} = H_b/R_c$ the aspect ratio and $f(\mathrm{Bo}_b, \mathrm{Bo}_e)$ a function of $\mathrm{Bo}_b = g\rho_g R_c^2/\gamma$, the buoyancy Bond number define by Eq. (7) and $\mathrm{Bo}_e = \varepsilon_0 E_0^2 R_c/2n\gamma$, the electrical Bond number define by Eq. (6). It is noteworthy that $n = 1$ in Bo_b (and was, therefore, omitted) as Bo_b accounts for the balance between the gravitational energy due to buoyancy and the capillary energy acting on a fully immersed bubble.

Despite the function $f(\mathrm{Bo}_b, \mathrm{Bo}_e)$ should be complex in general (i.e., for floating bubble at any Bo_b), the observations made on the energies in the last subsection suggest that the function could be simpler in specific cases (i.e., for floating bubble of intermediate Bo_b). To ascertain this insight the data from Fig. 6 are presented in Fig. 7 as a relation between Ar and Bo_e, for both solid (in red) and liquid substrates (in green, orange and mauve). As expected, the initial aspect ratio depends only on the size of the bubble, which is represented in Eq. (8) by the Bo_b. A linear law inspired by Eq. (1) is best adjusted with

$$\mathrm{Ar}(\mathrm{Bo}_b, \mathrm{Bo}_e) = A(\mathrm{Bo}_b) + \frac{9}{4}\mathrm{Bo}_e, \tag{9}$$

where $A(\mathrm{Bo}_b) = \mathrm{Ar}(\mathrm{Bo}_b, \mathrm{Bo}_e = 0)$ is the only fitting parameter, which is related to the initial aspect ratio and depends only on Bo_b. The corresponding laws, with $n = 3$, are drawn in Fig. 7 for each size of floating bubbles in the corresponding color. For sessile bubbles, the law $\mathrm{Ar} = 1 + 9/4\,\mathrm{Bo}_e$ with $n = 2$ (similar to the one used in Fig. 5) is also represented by a black solid line for the comparison. The $\mathrm{Ar}(\mathrm{Bo}_b, 0)$ found are in pretty good agreement with the predicted ones [36] (see Table I). Furthermore, for the studied range of bubble sizes, the changes of the aspect ratio due to E_0 are similarly described, for both floating and sessile bubbles, by the newly defined energy balance Bo_e. It is particularly clear when sessile bubbles (in red) and floating bubbles of $V_g = 0.25$ ml (in mauve) are compared in Fig. 7. For example, the energy ratio needed to start the Taylor cone Bo_e^* is the same in both cases. Moreover, the linear correlation given by Eq. (9) leads to good approximations of our results when the deformations are small.

In Fig. 8, the variation of the aspect ratio $\Delta\mathrm{Ar} = \mathrm{Ar}(\mathrm{Bo}_e, \mathrm{Bo}_b) - \mathrm{Ar}(\mathrm{Bo}_b, 0)$ is drawn as a function of Bo_e for both sessile (in red) and floating (in green, orange and mauve) bubbles. The $\Delta\mathrm{Ar}$ are obtained by subtracting the corresponding $A(\mathrm{Bo}_b)$ to each data set. In so doing, all data collapse on a single master curve allowing us to write

$$\mathrm{Ar}(\mathrm{Bo}_b, \mathrm{Bo}_e) = A(\mathrm{Bo}_b) + f_s(\mathrm{Bo}_e), \tag{10}$$

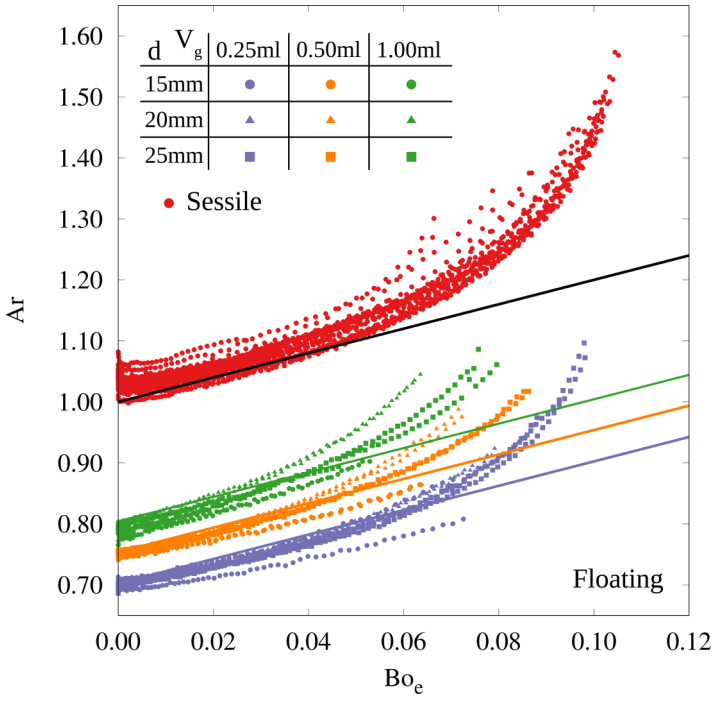

FIG. 7. Aspect ratio of floating bubbles $\mathrm{Ar} = H_b/R_c$ drawn as a function of the energy ratio $\mathrm{Bo}_e = \varepsilon_0 E_0^2 R_c/2n\gamma$. The same three sizes of capacitors d were used: $d = 15$ mm (solid circles), 20 mm (solid triangles) and 25 mm (solid squares), as well as the same three internal volumes V_g: $V_g = 0.25$ ml (in mauve), 0.50 ml (in orange), and 1.00 ml (in green). The straight lines correspond to Eq. (9) describing small deformations. The color of each line is linked to the corresponding V_g and the only fitting parameter for each curve is the aspect ratio in absence of field. The results for bubble resting on solid substrate (red solid circles) as well as the corresponding law (black straight line) are drawn for the sake of comparison.

with $A(\mathrm{Bo}_b)$ a function of Bo_b, that fully describes the initial shape of the bubbles [obtained by adjusting the Eq. (9)] and $f_s(\mathrm{Bo}_e)$ a function of Bo_e which describes how those initial shapes are modified by the electric field [see Eq. (4)].

Equation (9) corresponds to a functions represented by Eq. (10) and can be rewritten to be plotted in Fig. 8 as

$$\Delta\mathrm{Ar}(\mathrm{Bo}_e) = \frac{9}{4}\mathrm{Bo}_e. \tag{11}$$

Equation (11) approximates all data for small deformations as shown by the black solid line in Fig. 8. Consequently, deformation of both sessile and floating bubbles under a uniform electric field are in general described by a function defined by Eq. (8). This function [see Eq. (9)] is determined in the case of the experiments described in this article (namely, for floating bubbles of intermediate Bo_b and $\xi \approx 1$).

As it was pointed out in the Sec. I, the mobility of the contact line, and accordingly the initial shape of the bubbles, are influenced by the substrate. Although the major impact of the initial shape on the deformation was already discussed in the last sections, the meniscus itself does not seem to be directly influenced by the electric field. Measurements made on floating bubbles indicated a constant height of the meniscus (predicted as a function of Bo_b [36]) according to the electric field. However, on sessile bubbles, the meniscus height slightly decreases when the electric field increases. This was expected as the deformation of a bubble from a hemispherical shape necessarily

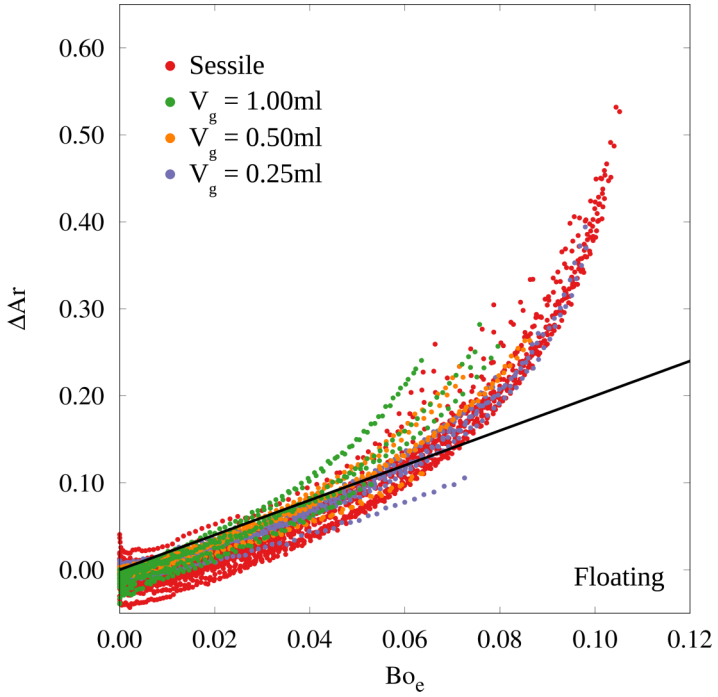

FIG. 8. Variation of the aspect ratio $\Delta \mathrm{Ar} = H_b/R_c - \mathrm{Ar}(\mathrm{Bo}_b, 0)$ of sessile (in red) and floating (in green, orange and mauve) bubbles drawn as a function of the energy ratio $Bo_e = \varepsilon_0 E_0^2 R_c/2n\gamma$. The same three internal volumes V_g: $V_g = 0.25$ ml (in mauve), 0.50 ml (in orange), and 1.00 ml (in green) were used. The straight line corresponds to the law given by the Eq. (11) describing small deformations.

comes with an increasing of the its surface. Consequently, liquid is needed to fuel the interface creation due to the deformation. This is not observed for floating bubbles since the liquid required is pumped in the tank of liquid. This observation is linked to the one done by Macky [33] on the lifetime of a bubble undergoing a Taylor cone. The absence of direct effect on the meniscus height can be understood thanks to the charges distribution at the interface. Indeed, as it has been showed numerically by Harris *et al.* [49], the charges distribution near the meniscus top (and therefore near the base of the hemisphere or the spherical cap formed by the bubble) is vanishing at any electric field. Accordingly, the observed absence of effect on meniscus is not surprising.

Nevertheless, although the meniscus carry a small amount of charges, it could have an effect on the general charges distribution on the bubble. Indeed, the Fig. 5 illustrated the good agreement between the experimental result presented here and the one presented in Ref. [17]. However, in the same paper, Basaran *et al.* demonstrated numerically the effect of the dimensionless drop size parameter (namely, the signed distance between the center the sphere formed by the droplet to the bottom electrode) on the critical electrical Bond number $\mathrm{Bo}^*_{e,s}$. During our experiments, for floating bubble of $V_g = 0.25$ ml, the $\mathrm{Bo}^*_{e,s} \sim 0.12$ (see Fig. 6). However, in Ref. [17] the predicted $\mathrm{Bo}^*_{e,s} \sim 0.26$, for a droplet with a drop size parameter equal to -0.5 (which correspond to the shape of a $V_g = 0.25$ ml bubble). This is more than twice what it was observed during the experiment. The corrections made on the capillary energy cannot explain this discrepancy. Nevertheless, the study by Harris *et al.* [49] on the effect of a nozzle on a hanging droplet can give an insight on the origin of this problem. Indeed, they showed that the nozzle increases the total charge carried by the droplet even when d was kept constant and when the charge directly carried by the nozzle it-self was small. As a consequence, the $\mathrm{Bo}^*_{e,s}$ decreases. Comparatively, the meniscus also carry a small amount of charge, but its shape is more complex than a cylindrical nozzle. Therefore, although a direct and

quantitative parallel is impossible due to the difference in shape, a qualitatively similar effect of the meniscus on the total charge carried could be conjectured. Accordingly, the presence of a meniscus at the base of the bubbles should reduce the $\mathrm{Bo}^*_{e,s}$ and explain the discrepancy between the numerical previsions [17] and the experimental result presented here.

The complete determination of the function describing the deformation of the bubbles under uniform electric field should thus evolve from a analysis similar to the one proposed in Ref. [49], but with a meniscus-shaped nozzle. However, unlike cylindrical nozzle, the meniscus have a shape imposed by the Bo_b [36]. This means that there is no need to add a dimensionless number to completely describe the system. Hence, the dimensional analysis and Eq. (8) remain valid, albeit the meniscus effect is added to the study.

VI. FRUSTRATED BUBBLES

Up to there, the liquid pool depth e was large enough and thus did not impact the bubble shape. Varying e may help to reveal a transition between floating and sessile bubbles by partially suppressing the immersed interface. Indeed, as floating bubbles have an immersed part, they also have a natural length of penetration h into the liquid as represented in Fig. 2(b). If the depth e becomes smaller than h, then the bottom electrode reaches the immersed interface and substitutes a part of this interface by a flat surface (solid if the liquid dewets the surface, liquid otherwise). The bubble becomes frustrated. Consequently, a smaller amount of energy is required to oppose the capillary energy. Therefore, at a given electric field, the deformation D should be larger. As explained in Sec. II, the depth e was controlled by changing the position of the bottom electrode. The minimum thickness that could be reached experimentally was $e \leqslant 0.20\,\mathrm{mm}$. In this limit case, the bubbles tend to move on the surface of the bath and have to be immobilized using, for example, nylon thread (since the threads are mostly immersed in the pool, they have no visible effect on the bubble dynamics).

As the penetration depth of the bubble was no longer prescribed by the Bo_b, but by an independent dimensional parameter e, a third dimensionless number is needed to describe the system. If the dimensionless depth of penetration e/R_c is chosen, then the shape of the bubble is fully describe by

$$\mathrm{Ar} = f_f(\mathrm{Bo}_b, \mathrm{Bo}_e, e/R_c), \tag{12}$$

with $\mathrm{Ar} = H_b/R_c$ the aspect ratio and $f_f(\mathrm{Bo}_b, \mathrm{Bo}_e, e/R_c)$ a function of $\mathrm{Bo}_b = g\rho_g R_c^2/\gamma$, the buoyancy Bond number define by Eq. (7), $\mathrm{Bo}_e = \varepsilon_0 E_0^2 R_c/2n\gamma$, the electrical Bond number define by Eq. (6) and e/R_c the dimensionless depth of penetration.

Figure 9 illustrates the aspect ratio Ar as a function of the energy ratio Bo_e. Bubbles of $V_g = 0.25\,\mathrm{ml}$, with a predicted $h = 1.38\,\mathrm{mm}$ [36], which was the largest achieved out of the three considered volumes, were measured using a capacitor of $d = 25\,\mathrm{mm}$. Measurements are sorted in three groups: the first one (Fig. 9, deep mauve) corresponds to $e \geqslant 1.25\,\mathrm{mm}$. The second category (Fig. 9, purple) corresponds to $e \approx 0.50\,\mathrm{mm}$. The third category (Fig. 9, pink) corresponds to $e \leqslant 0.20\,\mathrm{mm}$. The blue and the red points correspond to the limit cases: deep liquid bath and solid surface, respectively.

The nonfrustrated bubbles, with $e \geqslant 1.25\,\mathrm{mm}$, deform exactly like those on a deep liquid bath. The bubbles from this category have a h smaller than or close to e and thus no significant change on the shape is observed. In contrast, the most frustrated ones, with $e \leqslant 0.20$ mm, behave differently. First, the adjusted initial aspect ratio A in Fig. 9 is larger when the depth is smaller: since the bottom electrode presses the bottom part of the bubble, its immersed volume is reduced. Consequently, as the total volume V_g is constant, the emerged volume increases, and so does the aspect ratio. Second, to obtain the same deformation as for a nonfrustrated bubble, smaller values of E_0 and consequently of Bo_e are needed. It is especially visible in the energy ratio needed to start the Taylor cone Bo^*_e. This effect is mainly due to an overestimation of the capillary energy. Indeed, the contribution of each interface to the capillary energy is estimated assuming spheroidal cap shapes. However, a substantial part of the immersed interface is replaced (in case of dewetting, which appears to be the

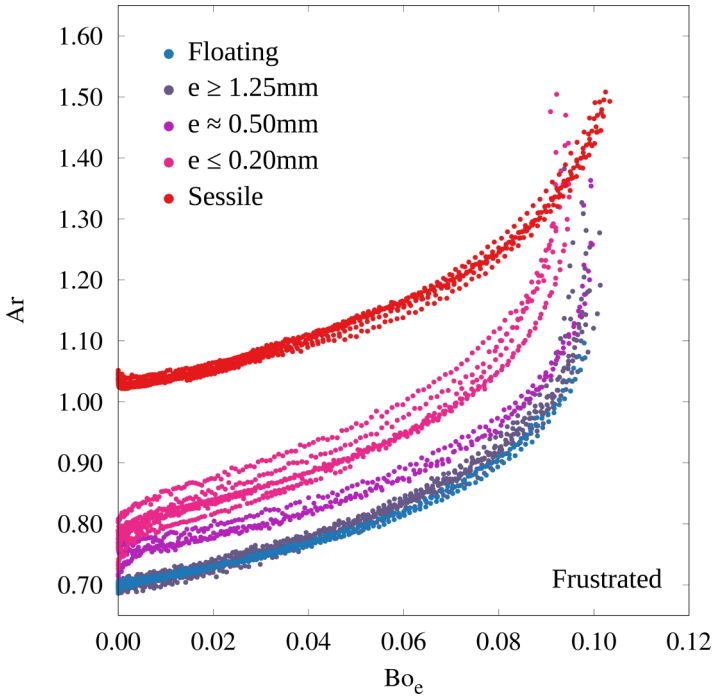

FIG. 9. Aspect ratio of frustrated bubbles $\mathrm{Ar} = H_b/R_c$ drawn as a function of the energy ratio $\mathrm{Bo}_e = \varepsilon_0 E_0^2 R_c/2n\gamma$ for different liquid depths e. The size of the capacitor is fixed to $d = 25$ mm and the internal volume to $V_g = 0.25$ ml. The blue and red circles correspond respectively to liquid and solid results in the same situation. The different results are sorted in three categories: $e \geqslant 1.25$ mm (in deep mauve), $e \approx 0.50$ mm (in purple), and $e \leqslant 0.20$ mm (in pink).

case) or flatted (otherwise) by the flat bottom electrode. Consequently, the capillary energy due to this interface is smaller. The total capillary energy calculation does not take this into account and is thus overestimated and so Bo_e is underestimated. Although the presence of a thin liquid film cannot be completely excluded without further investigations, frustrating the bubbles seems to lead to the dewetting of their bottom part. This is especially visible when frustrated bubbles blew up. Despite it does not affect the energy calculation, the presence of the thin film should nevertheless influence directly the mobility of the contact line. This is still an open question and further investigations are needed to address it.

In Fig. 9, the bubbles from the intermediate group ($e \approx 0.50$ mm) have an adjusted initial aspect ratio A between the one of the most frustrated and the nonfrustrated bubbles. However, for $\mathrm{Bo}_e \to \mathrm{Bo}_e^*$, the values of Ar are similar to those of nonfrustrated bubble. This transition from a behavior between most frustrated and nonfrustrated bubbles to another similar to that of nonfrustrated bubble is likely due to the decrease of the immersed surface influenced by the flat solid electrode. Indeed, when the bubble is deformed by an electric field, besides of the increase of the height H_b, there is also a stretching of R_b and therefore a decrease of R_c. This leads to the decreasing of the fraction of the immersed surface frustrated by the bottom electrode. Therefore, the approximate contribution of the immersed interface to the capillary energy becomes closer to the exact one.

If we analyze how to behave the frustrated bubbles, then we observe that, no matter how small e is, the frustrated bubbles have a behavior closer to the floating bubbles than to the sessile ones. Indeed, the adjusted initial aspect ratio A of most frustrated bubbles differs from that of a sessile bubble. This means that even a small thickness of liquid e is enough to change from a hemispherical shape with $\theta = 90^\circ$ (characteristic for sessile bubbles) to a spherical cap shape with $\theta \sim 60^\circ$

(characteristic for floating bubbles). This is due to the mobility of the contact line of the floating bubbles, which is pulled outwards by the surrounding liquid. The behavior of those frustrated bubbles illustrates the strong impacts of both the immersed interface on the energy ratio and the mobility of the contact line on the adjusted initial aspect ratio A. Besides the intrinsic differences between sessile and floating bubbles, our study confirms that the energy formulation and the aspect ratio have to be adapted to take into account the immersed interface and the contact line mobility of a floating bubble.

VII. CONCLUSION

In this paper, the deformation of a bubble induced by a vertical uniform electric field was measured when the bubble was resting on a solid and dry substrate or was floating on a bath. For bubbles resting on a solid and for large bubble floating on liquid ($\mathrm{Bo}_b > 100$ [36]), the bubbles are hemispherical and the bottom interface is flat. When the electric field is applied, the aspect ratio of the bubble evolves according to Eq. (1) found in Ref. [17]. However, for intermediate size of floating bubble ($2 < \mathrm{Bo}_b < 100$ [36]), the interface between the bath and the bubble has to be taken into account. The deformation law due to the electric field is similar to Eq. (1) under the following conditions: (i) the modification of the aspect ratio definition to account of the shape of the bubble that depends on the volume of the bubble and (ii) the modification of the electrical Bond number to account on the additional capillary pressure due to the bath-bubble interface. Floating bubbles had been also frustrated by controlling the depth of the bath. In so doing, the modifications to the law Eq. (1) was demonstrated robust and justified.

ACKNOWLEDGMENTS

S.D. thanks Fonds de la recherche scientifique–FNRS for financial support as Senior Research Associate. S.M., H.C., and S.D., thank the members of the AGEM (Michel Colin, Olivier Leboutte (former), Médéric Melard, Olivier Milis, and Samuel Rondia) for their help in improving the experimental setup as well as for their advice.

[1] J. D. Sartor, Electricity and rain, Phys. Today **22**(8), 45 (1969).
[2] C. T. R. Wilson, Some thundercloud problems, J. Franklin Inst. **208**, 1 (1929).
[3] C. T. R. Wilson, A theory of thunder cloud electricity, Proc. R. Soc. London A **236**, 297 (1956).
[4] W. A. Macky, Some investigations on the deformation and breaking of water drops in strong electric fields, Proc. R. Soc. London A **133**, 565 (1931).
[5] J. J. Nolan and J. G. O'Keeffe, Electric discharge from water drops, Math. Proc. R. Ir. Acad. **40**, 86 (1932).
[6] Lord Rayleigh, The influence of electricity on colliding water drops, Proc. R. Soc. London **28**, 406 (1879).
[7] Lord Rayleigh, On the equilibrium of liquid conducting masses charged with electricity, Philos. Mag. **14**, 184 (1882).
[8] D. Duft, H. Lebius, B. A. Huber, C. Guet, and T. Leisner, Shape Oscillations and Stability of Charged Microdroplets, Phys. Rev. Lett. **89**, 084503 (2002).
[9] D. Duft, T. Achtzehn, R. Müller, B. A. Huber, and T. Leisner, Rayleigh jets from levitated microdroplets, Nature **421**, 128 (2003).
[10] A. Pelesz, Charging of a single soap bubble, Przegl. Elektrotech. **94**, 176 (2018).
[11] J. Zeleny, On the condition of instability of electrified drops, with application to the electrical discharge from liquid point, Math. Proc. Cambridge Philos. Soc. **18**, 71 (1915).
[12] J. Zeleny, Instability of electrified liquid surfaces, Phys. Rev. **10**, 1 (1917).
[13] J. Zeleny, The role of surface instability in electrical disharge from drops of alcohol and water in air at atmospheric pressure, J. Franklin Inst. **219**, 659 (1935).
[14] G. I. Taylor, Disintegration of water drops in an electric field, Proc. R. Soc. London A **280**, 383 (1964).

[15] O. A. Basaran and L. E. Scriven, Axisymmetric shapes and stability of isolated charged drops, Phys. Fluids A **1**, 799 (1989).
[16] O. A. Basaran and L. E. Scriven, Axisymmetric shapes and stability of charged drops in an external electric field, Phys. Fluids A **1**, 795 (1989).
[17] O. A. Basaran and L. E. Scriven, Axisymmetric shapes and stability of pendant and sessile drops in an electric field, J. Colloid Interface Sci. **140**, 10 (1990).
[18] J. Beroz, A. J. Hart, and J. W. M. Bush, Stability Limit of Electrified Droplets, Phys. Rev. Lett. **122**, 244501 (2019).
[19] B. W. Wagoner, P. M. Vlahovska, M. T. Harris, and O. A. Basaran, Electric-field-induced transitions from spherical to discocyte and lens-shaped drops, J. Fluid Mech. **904**, R4 (2020).
[20] A. Marin, The saturnian droplet, J. Fluid Mech. **908**, F1 (2020).
[21] Q. Brosseau and P. M. Vlahovska, Streaming from the Equator of a Drop in an External Electric Field, Phys. Rev. Lett. **119**, 034501 (2017).
[22] K. J. Ptasinski and P. J. A. M. Kerkhof, Electric field driven separations: Phenomena and applications, Sep. Sci. Technol. **27**, 995 (1992).
[23] W. Dong, R. Li, H. Yu, and Y. Yan, An investigation of behaviours of a single bubble in a uniform electric field, Exp. Therm. Fluid Sci. **30**, 579 (2006).
[24] M. Cloupeau and B. Prunet-Foch, Electrostatic spraying of liquids in cone-jet mode, J. Electrostat. **22**, 135 (1989).
[25] M. Cloupeau and B. Prunet-Foch, Electrostatic spraying of liquids: Main functioning modes, J. Electrostat. **25**, 165 (1990).
[26] R. Collins, J. J. Jones, M. T. Harris, and O. A. Basaran, Electrohydrodynamic tip streaming and emission of charged drops from liquid cones, Nat. Phys. **4**, 149 (2008).
[27] Y. Shin, M. Hohman, M. Brenner, and G. Rutledge, Experimental characterization of electrospinning the electrically forced jet and instabilities, Polymer **42**, 09955 (2001).
[28] J.-U. Park, M. Hardy, S. J. Kang, K. Barton, K. Adair, D. K. Mukhopadhyay, C. Y. Lee, M. S. Strano, A. Alleyne, J. G. Georgiadis, P. M. Ferreira, and J. A. Rogers, High-resolution electrohydrodynamic jet printing, Nat. Mater. **6**, 782 (2007).
[29] M. Gamero-Castaño and V. Hruby, Electrospray as a source of nanoparticles for effcient colloid thrusters, J. Propuls. Power **17**, 977 (2001).
[30] I. G. Loscertales, A. Barrero, I. Guerrero, R. Cortijo, M. Marquez, and A. M. Gañán-Calvo, Micro/nano encapsulation via electrified coaxial liquid jets, Science **295**, 1695 (2002).
[31] K. Kataria, A. Gupta, G. Rath, R. Mathur, and S. R. Dhakate, *In vivo* wound healing performance of drug loaded electrospun composite nanofibers transdermal patch, Int. J. Pharm. **469**, 102 (2014).
[32] C. T. R. Wilson and G. I. Taylor, The bursting of soap-bubbles in a uniform electric field, Math. Proc. Cambridge Philos. Soc. **22**, 728 (1925).
[33] W. A. Macky, Deformation of soap bubbles in electric fields, Math. Proc. Cambridge Philos. Soc. **26**, 421 (1930).
[34] J. E. Hilton and A. van der Net, Dynamics of charged hemispherical soap bubbles, Europhys. Lett. **86**, 24003 (2009).
[35] D. E. Moulton and J. A. Pelesko, Theory and experiment for soap-film bridge in an electric field, J. Colloid Interface Sci. **322**, 252 (2008).
[36] M. A. C. Teixeira, S. Arscott, S. J. Cox, and P. I. C. Teixeira, What is the shape of an air bubble on a liquid surface? Langmuir **31**, 13708 (2015).
[37] O. Bonhomme, O. Liot, A.-L. Biance, and L. Bocquet, Soft Nanofluidic Transport in a Soap Film, Phys. Rev. Lett. **110**, 054502 (2013).
[38] A. Pelesz and P. Zylka, On analytical and experimental aspects of soap bubble stream charging, Exp. Fluids **61**, 241 (2020).
[39] K. Golemanov, N. D. Denkov, N. D. Tcholakova, M. Vethamuthu, and A. Lips, Surfactant mixtures for control of bubble surface mobility in foam studies, Langmuir **24**, 9956 (2008).
[40] J. D. Berry, M. J. Neeson, R. R. Dagastine, D. Y. Chan, and R. F. Tabor, Measurement of surface and interfacial tension using pendant drop tensiometry, J. Colloid Interface Sci. **454**, 226 (2015).

[41] J. Miguet, Amincissement et stabilité de bulles de surface, Ph.D. thesis, Université Paris Saclay (2019).
[42] C. Cohen, B. D. Texier, E. Reyssat, J. H. Snoeijer, D. Quéré, and C. Clanet, On the shape of giant soap bubbles, Proc. Natl. Acad. Sci. USA **114**, 2515 (2017).
[43] S. D. Pawar, P. Murugavel, and D. M. Lal, Effect of relative humidity and sea level pressure on electrical conductivity of air over indian ocean, J. Geophys. Res. **114**, D02205 (2009).
[44] J. R. Melcher and G. I. Taylor, Electrohydrodynamics: A review of the role of interfacial shear stresses, Annu. Rev. Fluid Mech. **1**, 111 (1969).
[45] A. Lukichev, Physical meaning of the stretched exponential Kohlrausch function, Phys. Lett. A **383**, 2983 (2019).
[46] G. I. Barenblatt, *Scaling, Self-Similarity, and Intermediate Asymptotics* (Cambridge University Press, Cambridge, UK, 1996).
[47] G. Liger-Belair, The physics behind the fizz in champagne and sparkling wines, Eur. Phys. J.: Spec. Top. **201**, 1 (2012).
[48] M. M. Wind, J. Vlieger, and D. Bedeaux, The polarizability of a truncated sphere on a substrate I, Physica A **141**, 33 (1987).
[49] M. T. Harris and O. A. Basaran, Capillary electrohydrostatics of conducting drops hanging from a nozzle in an electric field, J. Colloid Interface Sci. **161**, 389 (1993).